Green Chemistry

PAPER

View Article Online
View Journal | View Issue

Cite this: *Green Chem.*, 2025, **27**, 15236

Trace-LiCl-assisted synthesis of high-loading ordered Pt_3Co intermetallic catalysts for the oxygen reduction reaction in fuel cells

Yutao Ni,[a,b] Jiahui Song,[a,b] Huiying Lan,[a] Xue Jing,[a,b] Wenwen Shi, *[a] Ruimin Ding*[a] and Xi Yin *[a]

Received 24th September 2025,
Accepted 29th October 2025

DOI: 10.1039/d5gc05077d

rsc.li/greenchem

The synthesis of high-loading platinum intermetallic compounds (IMCs) for proton exchange membrane fuel cells (PEMFCs) remains challenging due to severe nanoparticle agglomeration and inhomogeneity during high-temperature annealing. Here, we report a trace lithium chloride (LiCl)-assisted strategy that enables the synthesis of highly ordered Pt_3Co IMCs with ultrahigh metal loading (50.43 wt% Pt) and a small particle size (~3.58 nm). Comprehensive characterization reveals that LiCl lowers the activation barrier for Pt/Co salt reduction by a strong polarization force, while its molten-salt phase accelerates Co diffusion into the Pt lattice and surface atomic rearrangement. The resulting Pt_3Co/C catalyst achieves a record oxygen reduction reaction (ORR) mass activity (MA) of 0.86 ± 0.04 A mg_{pt}^{-1} in rotating disk electrode (RDE) tests. When integrated into PEMFC cathodes, it delivers peak power densities (PPD) of 2.92 W cm^{-2} (H_2–O_2) and 1.23 W cm^{-2} (H_2–air) at 80 °C, alongside exceptional stability. Crucially, the MA at 0.9 V reaches 0.61 A mg_{pt}^{-1}, surpassing the U.S. DOE 2025 target (0.44 A mg_{pt}^{-1}) by 39%. This work pioneers a barrier-lowering synthesis paradigm that resolves the fundamental ordering–sintering trade-off in high-temperature IMC fabrication.

Green foundation

1. This work presents a sustainable method for synthesizing high-loading Pt_3Co intermetallic catalysts. Using trace LiCl molten salt lowers reduction barriers and facilitates alloying, enabling the rapid formation of highly ordered Pt_3Co at 700 °C in just 2 hours while effectively suppressing particle agglomeration.
2. The synthesized Pt_3Co catalyst features a high Pt loading (~50.43 wt%), a small particle size (~3.58 nm), and an ordered structure. In proton exchange membrane fuel cells, it achieves high power densities (2.92 W cm^{-2} in H_2–O_2; 1.23 W cm^{-2} in H_2–air) and demonstrates excellent durability with minimal activity loss (19.3%) after 30 000 cycles, exceeding the 2025 DOE targets.
3. Future research could tune energy barriers by controlling molten salt polarization, establishing design principles for intermetallic synthesis. This guides scalable production of advanced catalysts, ultimately accelerating the commercialization of next-generation PEMFC technologies.

1. Introduction

Proton exchange membrane fuel cells (PEMFCs) efficiently convert chemical energy into electrical energy with zero direct emissions, positioning them as key technologies for addressing global energy challenges.[1–3] However, the sluggish kinetics of the oxygen reduction reaction (ORR) necessitate substantial Pt consumption to ensure reliable performance and stability, thus hindering the large-scale application of PEMFCs.[4,5] Pt-based intermetallic compounds (PtM-IMCs), formed by alloying Pt with transition metals (such as Co, Fe, Ni, *etc.*), have emerged as promising alternative catalysts with reduced Pt requirements due to their enhanced ORR activity.[6,7]

Experimental and theoretical studies confirm that ordered Pt_3Co IMCs exhibit enhanced lattice contraction and strong orbital coupling effects, collectively enhancing intrinsic ORR activity and structural stability.[8–12] However, achieving atomic ordering necessitates high-temperature treatment (≥700 °C) to overcome the kinetic barriers for atomic diffusion and rearrangement,[13–15] inevitably inducing severe nanoparticle sintering. Current strategies to mitigate nanoparticle sintering primarily leverage protective encapsulation and enhanced support–catalyst interactions. Protective encapsulation

[a]*State Key Laboratory of Coal Conversion, Institute of Coal Chemistry, Chinese Academy of Sciences, Taiyuan, Shanxi 030001China. E-mail: shiwenwen@sxicc.ac.cn, dingrm@sxicc.ac.cn, xiyin@sxicc.ac.cn*
[b]*School of Chemical Engineering, University of Chinese Academy of Sciences, Beijing 100049, China*

achieved by coating Pt alloy clusters with carbonized polymers or sacrificial SiO_2/TiO_2/MgO physically confines particles during high-temperature annealing, yielding small-sized IMCs (~1.5 nm).[7,16–20] Complementarily, engineered carbon supports doped with heteroatoms (B, N, O, F, and S) exploit strong Pt–support electronic interactions to stabilize sub-5 nm IMCs below 1000 °C.[21–27] Additionally, hierarchically porous carbon supports provide spatial confinement through their tunable pore structures, further restricting particle mobility and coalescence.[28,29] Nevertheless, these approaches remain largely limited to low metal loadings (~20 wt% Pt).

High-loading PtM-IMC/C catalysts are technologically relevant for PEMFCs, enabling thin catalytic layers with enhanced electron conductivity and rapid mass transport.[30,31] However, decreased interparticle distance at high Pt loading exacerbates sintering susceptibility.[32] To address this limitation, a seed-mediated method (using 20 wt% Pt_3Co/C as the crystalline seeds) has been developed for synthesizing a Pt_3Co/C catalyst with 40 wt% Pt content, yielding particles averaging 7.1 ± 0.8 nm.[30] Alternatively, a CoO_x-assisted strategy enables structural evolution from ultrafine Pt nanocrystals to sub-6 nm core–shell PtCo intermetallic compound structures (~44.7 wt% Pt), where Co^{3+} ions (Pt : Co = 1 : 1) were deposited as Co_3O_4 generates oxygen vacancies that drive Pt/Co inter-diffusion while spatially suppressing sintering.[33] Despite achieving high Pt loading, both methods produce particle sizes exceeding the optimal 3–4 nm range,[34–36] compromising Pt utilization efficiency.[37]

To resolve the fundamental trade-off between ordering degree and particle size, we introduce a trace-LiCl-assisted approach. While conventional molten salts lower reaction barriers and accelerate mass transfer,[38,39] excessive amounts trigger uncontrolled particle coarsening, ultimately degrading crystallinity. Our approach leverages trace LiCl to engineer a finely modulated environment. Its content generates sufficient polarizing interactions to disrupt Pt/Co salt bonding and lower its reduction energy barriers. Simultaneously, its molten phase promotes the incorporation of cobalt atoms into the platinum lattice and rearranges surface atoms during Pt_3Co formation, ultimately enhancing its long-range atomic order. Crucially, this approach employs high-temperature (700 °C) short-duration (2 h) heat treatment to restrict grain migration and growth, while the molten LiCl promotes atomic alloying and ordering. This dual functionality overcomes the persistent dilemma between the high temperature required for ordering and the unavoidable thermal agglomeration. Comprehensive characterization confirms that trace LiCl promotes Pt_3Co (50.43 wt% Pt) alloying and atomic ordering, yielding highly ordered catalysts with uniform 3.58 ± 0.02 nm particles. The optimized Pt_3Co catalyst demonstrates exceptional ORR performance and excellent stability, exhibiting a mass activity (MA) of 0.61 A mg_{Pt}^{-1}, which only decreases 19.3% after 30k-cycle accelerated stress testing (AST). It achieves a peak power density (PPD) of 1.23 W cm^{-2} (H_2–air) and an 11.6% decline after 30k-cycle AST in a fuel cell, exceeding the Department of Energy (DOE) 2025 target.[2]

2. Experimental

2.1 Materials

Chloroauric acid hexahydrate ($H_2PtCl_6{\cdot}6H_2O$, ≥37.5%, Sigma–Aldrich), cobalt(II) chloride ($CoCl_2$, 99.7%, Macklin), lithium chloride (LiCl, ≥99%, Aladdin), hydrochloric acid (HCl, 36.0%–38.0%, high purity, SCR, China), perchloric acid ($HClO_4$, 70%, Thermo Fisher Scientific), carbon black (Black Pearl 2000, Cabot Co), Pt/C (46.5 wt% Pt, TEC10E50E, Tanaka Kikinzoku Kogyo K K), Nafion D521 dispersion (5 wt%, EW = 1100, Alfa Aesar), isopropanol (IPA, >99.7%, analytical reagent grade, Kermel), deionized water (DI water, Milli-Q, 18.2 MΩ cm at 25 °C), ultrapure nitrogen (N_2, 99.999%), ultrapure oxygen (O_2, 99.999%), hydrogen/argon mixture (5 vol% H_2 in Ar), synthetic air (CO_2-free), Nafion membranes (18 μm, Gore), gas diffusion layer (GDL, Sigracet 22BB, 215 μm, SGL Carbon), and fiber-reinforced polytetrafluoroethylene gasket (PTFE, 150 μm) were used as received.

2.2 Synthesis of Pt_3Co/C(Li_x) catalysts

Pt_3Co/C(Li_x) catalysts with varying Li content (Pt : Co : Li atomic ratios = 3 : 1 : x, where x = 0.0, 0.3, 0.5, 0.6, 0.7, and 1.0) were synthesized *via* a trace-LiCl-assisted method. The target Pt loading was 50 wt% Pt. Stock solutions were first prepared by dissolving $H_2PtCl_6{\cdot}6H_2O$ (10 g) in DI water and diluting to 100 mL to obtain 0.193 M H_2PtCl_6, and separately dissolving $CoCl_2$ (3.246 g) in concentrated HCl (117 μL), followed by dilution to 250.0 mL with DI water to yield 0.1 M $CoCl_2$. For catalyst preparation, carbon black (188.3 mg) was dispersed in DI water (150.0 mL) *via* vacuum impregnation at room temperature until bubble-free, and then stirred at 350 rpm for 20 h. Concurrently, LiCl (0.0, 4.2, 7.1, 8.5, 9.9, and 14.1 mg) was dissolved in DI water (17.5 mL). The Pt stock solution (5.0 mL) and Co stock solution (3.2 mL) were added to the LiCl solution, and the mixture was sonicated for 10 min. This metal precursor solution was added dropwise to the stirred carbon dispersion. The resulting slurry was stirred at 350 rpm for 16 h and freeze-dried (−15 °C, ~0.5 Pa). The dried precursor was thermally treated under flowing H_2/Ar.

For the main catalyst series (all x values = 0.0–1.0), the precursors were heated to 700 °C at 10 °C min^{-1}, held for 2 h, and cooled to ambient temperature. These catalysts are denoted as Pt_3Co/C(Li_x)-700 °C-2 h. To investigate the role of LiCl in Pt_3Co atomic ordering evolution, a separate series was prepared. The dried precursors (x = 0.0 and 0.6) were subjected to the same heating ramp (10 °C min^{-1}) to target temperatures (200, 300, 400, 500, 600, and 700 °C) and were immediately cooled upon reaching each target temperature (without hold time). These samples are labeled as Pt_3Co/C(Li_x)-T, where T represents the target temperature.

2.3 Characterization

The X-ray diffraction (XRD) patterns were obtained using a Rigaku Smart Lab SE diffractometer equipped with a Cu-Kα source (λ = 0.15406 nm), operated at 40 kV and 40 mA, to deter-

mine the crystalline phase and structure of the samples. Transmission electron microscopy (TEM, JEM-2100F, JEOL, Japan, 200 kV) was used to analyze the morphology. Aberration-corrected high-angle annular dark-field scanning transmission electron microscopy (HAADF-STEM, FEI Themis Z, Titan Cubed Themis G2300, JEM-ARM200F, 300 kV) was used to analyze the unit cell structure. X-ray photoelectron spectroscopy (XPS) analysis was conducted on a Thermo Scientific system with a monochromatic Al Kα X-ray source ($h\nu$ = 1486.6 eV) operating at 72 W to analyze the surface elemental composition and chemical states. The bulk chemical composition of the catalysts was determined using inductively coupled plasma-optical emission spectrometry (ICP-OES) with a PerkinElmer NexION 5000 spectrometer. X-ray absorption spectroscopy (XAS) measurements were performed at the BL14W1 of the Shanghai Synchrotron Radiation Facility (SSRF) in transmission or fluorescence mode to probe the local atomic structure, oxidation states, and coordination environment of specific elements. Additionally, X-ray fluorescence (XRF) analysis was conducted using a Thermo Scientific ARL QUANT X spectrometer to assess the bulk elemental composition.

2.4 Electrochemical measurements of $Pt_3Co/C(Li_x)$ catalysts

Before conducting electrochemical and membrane electrode assembly (MEA) tests, the catalysts were thoroughly rinsed with DI water to remove residual LiCl and then dried overnight under vacuum at 60 °C. The catalyst inks were prepared by dispersing 2.0 mg of catalyst powder in a mixture of DI water (500 μL), IPA (500 μL), and D521 Nafion dispersion (5.0 μL, 5 wt%). The mixture was sonicated in an ultrasonic bath for 40 min to ensure uniform dispersion. A Pt mass loading of 30 μg_{Pt} cm^{-2} was prepared by depositing 5.9 μL of the ink onto the working electrodes.

Electrochemical measurements were performed using a standard three-electrode system controlled by a Pine Research MSR rotator (Pine Research Instrumentation Co., Ltd, USA) coupled to a bipotentiostat (CHI 760E, CH Instruments, Inc., China). A rotating disc electrode (RDE, Pine Research Instrumentation) with a glassy carbon disk (Φ = 5.0 mm) served as the working electrode. A graphite rod and a reversible hydrogen electrode (RHE) were used as the counter and reference electrodes, respectively. Staircase cyclic voltammetry (SCV, *iR*-compensated) curves were measured by polarizing the working electrode from 1.1 to 0 V *vs.* RHE, employing 20 mV potential steps and a hold time of 2 s at each step at a rotation speed of 1600 rpm in O_2-saturated 0.1 M $HClO_4$ solution. Prior to SCV measurements, the catalysts were activated by performing 20 cyclic voltammetry (CV) cycles at a scan rate of 50 mV s^{-1} in N_2-saturated 0.1 M $HClO_4$. The hydrogen desorption region of the 20th CV cycle was used to calculate the electrochemically active surface area (ECSA). Accelerated degradation testing (ADT) involved 20 000 cycles in N_2-saturated 0.1 M $HClO_4$ between 0.6 and 0.95 V *vs.* RHE at a scan rate of 100 mV s^{-1}.

The ECSA of Pt was calculated using the following equation:

$$\mathrm{ECSA} = \frac{Q_H}{0.21 \times m_{pt}} \quad (1)$$

where Q_H (mC) represents the hydrogen desorption charge, obtained by integrating the low-potential region (0.05–0.45 V *vs.* RHE) of the double-layer-corrected CV; 0.21 (mC cm^{-2}) is the charge required for monolayer hydrogen adsorption on a smooth polycrystalline Pt surface; and m_{Pt} (μg_{Pt} cm^{-2}) denotes the Pt mass loading on the working electrode.

The kinetically limited current density (j_k) was calculated using the Koutecky–Levich equation:

$$\frac{1}{j} = \frac{1}{j_k} + \frac{1}{j_d} \quad (2)$$

where j (mA cm^{-2}) is the *iR*-corrected current density and j_d (mA cm^{-2}) is the limiting current density.

The MA and specific surface area activity (SA) were determined using the following equation:

$$\mathrm{MA} = \frac{j_k}{m_{Pt}} \quad (3)$$

$$\mathrm{SA} = \frac{\mathrm{MA}}{\mathrm{ECSA}} \quad (4)$$

2.5 Single-cell fabrication and testing

Single-cell MEAs with a 5 cm^2 active area were fabricated using the catalyst-coated membrane (CCM) method. Commercial Pt/C was used exclusively as the anode catalyst, whereas the synthesized $Pt_3Co/C(Li_{0.0})$-700 °C-2 h and $Pt_3Co/C(Li_{0.6})$-700 °C-2 h electrocatalysts served as the cathode catalysts.

The commercial Pt/C ink was prepared by ultrasonically homogenizing a mixture of catalyst powder (4.34 mg), DI water (0.594 mL), IPA (0.756 mL), and a 5% D521 Nafion ionomer solution (30.06 μL) for 40 min. The $Pt_3Co/C(Li_{0.0})$-700 °C-2 h ink was prepared by ultrasonically homogenizing a mixture of catalyst powder (4.00 mg), DI water (1.174 mL), IPA (1.496 mL), and a 5% D521 Nafion ionomer solution (25.81 μL) for 150 min. The $Pt_3Co/C(Li_{0.6})$-700 °C-2 h ink was prepared by ultrasonically homogenizing a mixture of catalyst powder (4.00 mg), DI water (1.174 mL), IPA (1.496 mL), and a 5% D521 Nafion ionomer solution (30.11 μL) for 150 min. CCMs were fabricated by ultrasonically spraying the anode ink onto a Nafion membrane at 80 °C on a vacuum plate, followed by spraying the cathode ink onto the opposite side. Pt loading was kept at 0.10 mg_{Pt} cm^{-2} on both the cathode and anode in the CCMs for fuel cell performance evaluation. Pt loading was kept at 0.33 mg_{Pt} cm^{-2} for the cathode and 0.20 mg_{Pt} cm^{-2} for the anode in the CCMs for AST. The actual loadings were confirmed by XRF analysis.

The MEAs were fabricated by sandwiching the CCM between two GDLs, with two fiber-reinforced PTFE gaskets positioned on the outer sides of the GDLs. These gaskets ensure that the GDLs are compressed to approximately 70% of

their original thickness. The MEAs were then assembled into single-cell fuel cell hardware (5 cm^2 single-channel serpentine flow field, graphite plates, Scribner Inc.). Cell bolts were tightened to a torque of 6 N m. The assembled cells were connected to a fuel cell test station (Scribner Associates Incorporated, 850e) for performance evaluation.

Polarization curves were recorded at 80 °C under the following conditions: potential was scanned from 1.0 to 0.2 V using 20 mV steps with a 20 s hold time at each step; the anode was supplied with fully humidified H_2 (500 sccm); the cathode was supplied with fully humidified O_2 (500 sccm) or air (2000 sccm); both anode and cathode compartments were maintained at 250 kPa_{abs}. CVs were recorded at 40 °C and 100 kPa_{abs} by scanning between 0.05 V and 1.2 V at 50 mV s^{-1}, with fully humidified H_2 and N_2 supplied to the anode (200 sccm) and cathode (200 sccm), respectively. The electrochemical impedance spectra (EIS) were measured at 0.1 and 1.2 A cm^{-2} in 0.1–20 000 Hz (80 °C, 100% RH, 150 kPa_{abs}, 500 sccm H_2, 500 sccm air). AST of the catalyst followed the US DOE protocols, employing square-wave potential cycling between 0.6 V and 0.95 V (with a 3 s hold at each potential) at 80 °C and under 100 kPa_{abs}. During AST, fully humidified H_2 (200 sccm) and N_2 (75 sccm) were supplied to the anode and cathode, respectively. Polarization curves and CV curves were recorded both before and after AST.

2.6 Ordering degree calculation

The characteristic XRD peaks observed at 23.06° and 32.84° correspond to the (100) and (110) crystal planes of the face-centered cubic (fcc) Pt_3Co structure. The long-range ordering degree (D) was calculated by comparing the integrated area ratio of the experimental (110)/(111 + 200) peaks with the reference intensity ratio from the standard Pt_3Co diffraction pattern (PDF#29-0499), as follows:[40]

$$D = \frac{S(110)/(S(111)+S(200))}{I(110)/(I(111)+I(200))} \times 100\% \quad (5)$$

where S refers to the integrated peak area of the experimental (hkl) reflection and I corresponds to the reference peak intensity of the (hkl) plane in Pt_3Co, PDF #29-0499.

3. Results and discussion

3.1 Effect of LiCl addition on the atomic ordering degree of Pt_3Co

To engineer a finely modulated environment for Pt_3Co formation, we prepared a series of $Pt_3Co/C(Li_x)$-700 °C-2 h (x = 0.0, 0.3, 0.5, 0.6, 0.7, 1.0) catalysts. Notably, the LiCl amount used in this study represents a trace addition. This is highlighted by comparison to typical molten-salt syntheses involving significantly larger quantities, such as the atomic ratio of Pt : Li = 1 : 47.2,[41] atomic ratio of Ti : (Li + K) = 1 : 2.9,[42] and atomic ratio of Co : (Li + K) = 1 : 21.2.[43] Comprehensive characterization (ICP, XRD, TEM, HAADF-STEM, XPS, and XAS) reveals systematic variations in the crystal and electronic structures with increasing x. ICP-OES confirms a consistent Pt loading of ~50 wt% for all samples (Table S1). XRD patterns (Fig. 1a) exhibit distinct characteristic peaks at 23.06°, 32.84°, 40.53°, and 47.12°, corresponding to the (100), (110), (111), and (200) crystal planes of the Pt_3Co standard (PDF #29-0499), respectively. The calculated D (Fig. 1b) demonstrates a volcano-type trend *versus* x, peaking at 53.38% for x = 0.6. This result indicates that optimal LiCl addition enhances the atomic ordering of Pt_3Co. TEM images (Fig. 1c and S1a–S5a) and EDS mapping (Fig. 1d and S1b–S5b) confirm particle distribution on the carbon black support and a homogeneous Pt and Co distribution within individual nanoparticles. Particle sizes increase progressively with x (Fig. 1b and S1a, S2c–S5c), from 3.11 ± 0.03 (x = 0.0), 3.20 ± 0.12 (x = 0.3), 3.31 ± 0.05 (x = 0.5), 3.58 ± 0.02 (x = 0.6), 3.63 ± 0.04 (x = 0.7) to 3.87 ± 0.16 nm (x = 1.0). $Pt_3Co/C(Li_{0.6})$-700 °C-2 h exhibits high D while also being among the smallest particles reported to date for IMCs (Table S2). To gain deeper structural insights into the catalysts with optimal (x = 0.6) and reference (x = 0.0) LiCl dosages, HAADF-STEM analysis was performed. Fig. 1e depicts a $Pt_3Co/C(Li_{0.6})$-700 °C-2 h nanoparticle oriented along the [001] zone axis. The atomic number (Z) contrast of HAADF-STEM results in higher intensity for Pt atomic columns compared to Co columns.[44,45] Analysis within the red boxed region reveals a central Co column surrounded by Pt columns positioned at the vertices and edges, forming a periodically ordered square lattice. Critically, a Pt-rich shell is evident at the nanoparticle edge (yellow box). This ordered structure in $Pt_3Co/C(Li_{0.6})$-700 °C-2 h is confirmed by the measured lattice spacings (Fig. 1e), fast Fourier transform (FFT) patterns (Fig. 1f), and alternating intensity line profiles (Fig. 1g). For the $Pt_3Co/C(Li_{0.0})$-700 °C-2 h control sample imaged along the [01$\bar{1}$] direction (Fig. S1d), the lattice spacings, FFT pattern (Fig. S1e), and alternating intensity profile (Fig. S1f) similarly confirm an ordered bulk structure. However, in contrast to the $Pt_3Co/C(Li_{0.6})$-700 °C-2 h sample, $Pt_3Co/C(Li_{0.0})$-700 °C-2 h exhibits no distinct Pt-rich shell formation at the edge.

XPS was performed to analyze the electronic structure of the $Pt_3Co/C(Li_x)$-700 °C-2 h catalyst. The Pt 4f spectra (Fig. S6a) reveal a consistent positive binding energy shift of 0.1 eV in LiCl-assisted samples *versus* the LiCl-free reference, indicative of a downshift of the d-band center.[33,46,47] Deconvolution analysis (Fig. 2a, b, S6b–f and Table S3) demonstrates dominant Pt^0 species (>50% composition) across all catalysts, with maximal metallic character at x = 0.6. XAS was further conducted to clarify the electronic state and the local coordination environment of the catalysts. At the Pt L_3-edge (Fig. 2c), both the x = 0.6 and x = 0.0 samples exhibit significantly reduced white-line (WL) intensity relative to PtO_2, approaching that of Pt foil, confirming a metallic Pt valence state.[48] Notably, the x = 0.6 sample displays enhanced oscillation intensity within the 11 576–11 584 eV range, indicative of superior long-range atomic ordering.[49] Fourier-transformed (FT) extended X-ray absorption fine structure (EXAFS) spectra of the Pt L_3-edge (Fig. 2d) reveal a prominent Pt–Co peak at near 2.45 Å. This bond length is markedly shorter than Pt–Pt in Pt foil (2.70 Å),

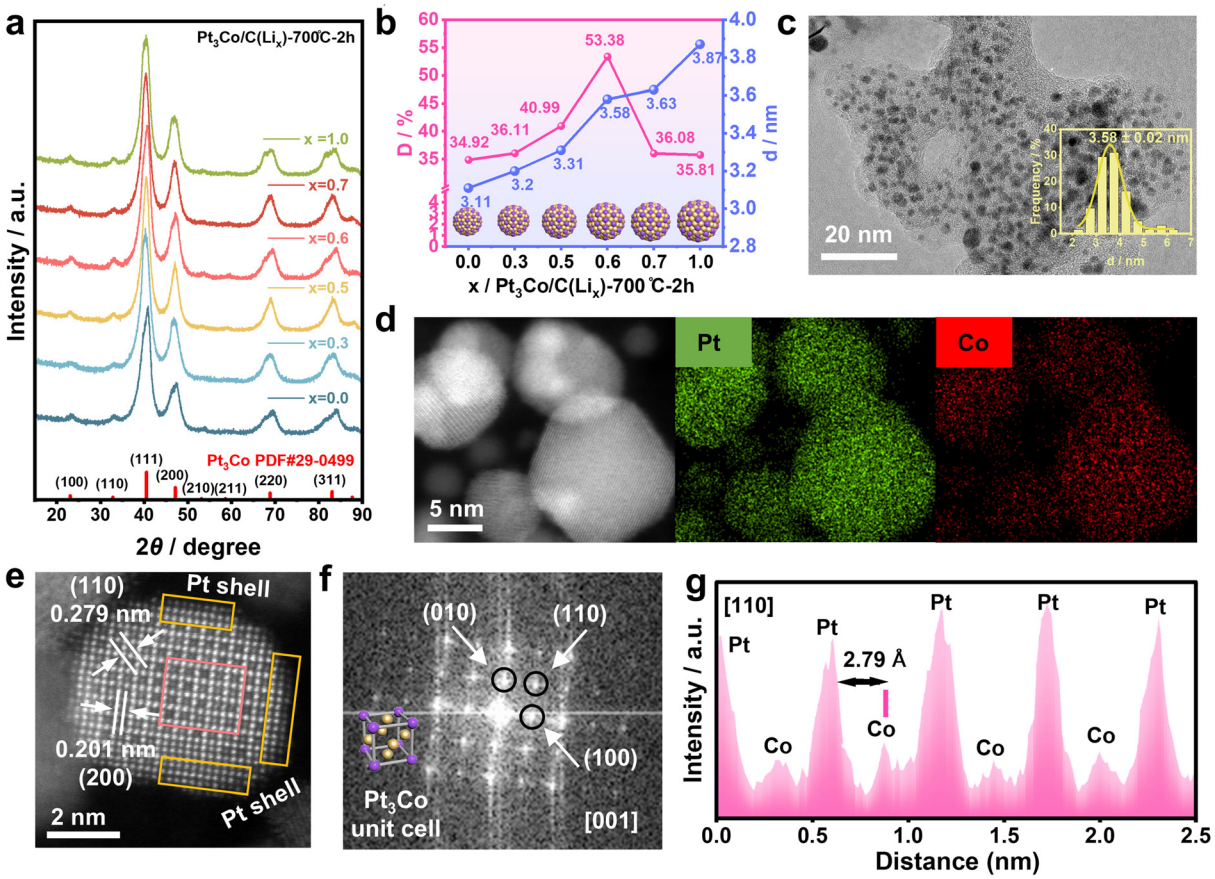

Fig. 1 Structural characterization of $Pt_3Co/C(Li_x)$-700 °C-2 h catalysts. (a) XRD patterns. (b) Histogram of ordering degree and particle size distribution. (c) TEM image of $Pt_3Co/C(Li_{0.6})$-700 °C-2 h. (d) EDS mapping images of $Pt_3Co/C(Li_{0.6})$-700 °C-2 h. (e) Atomic-resolution HAADF-STEM image of $Pt_3Co/C(Li_{0.6})$-700 °C-2 h. (f) FFT pattern of the highlighted area in (e). (g) Alternating intensity line profile corresponding to (e).

consistent with the compressive strain within the Pt_3Co-IMCs. The significantly higher Pt–Co peak intensity for the x = 0.6 sample compared to the x = 0.0 reference further corroborates its enhanced structural ordering. Quantitative EXAFS fitting analysis (Fig. S7 and Table S4) reveals distinct coordination environments. For the x = 0.0 catalyst, fitting identifies Pt–O, Pt–Co, and Pt–Pt contributions. In contrast, the x = 0.6 catalyst shows Pt–Co and Pt–Pt, with a lesser Pt–O contribution. This absence of Pt–O coordination signifies further reduction to the metallic state and a purified Pt surface. The increased Pt–Co coordination number (CN) in x = 0.6 (CN = 1.56) *versus* x = 0.0 (CN = 1.27) confirms strengthened heteroatomic ordering. Wavelet transform (WT) analysis of Pt L_3-edge EXAFS oscillations (Fig. 2e) demonstrates maximum intensities at 9.58 $Å^{-1}$ (x = 0.0) and 9.60 $Å^{-1}$ (x = 0.6), both significantly shifted from Pt foil (11.32 $Å^{-1}$). This shift confirms the dominant contribution of Pt–Co scattering paths. Co K-edge spectra (Fig. 2f) reveal reduced intensity relative to Co_3O_4 and a shift toward metallic Co foil, demonstrating predominant Co^0 participation in the alloy. Intensified oscillations at 7745–7755 eV for the x = 0.6 sample further corroborate ordering enhancement. Consistently, the FT-EXAFS spectra (Fig. 2g and S8) reveal an increased Pt–Co coordination peak at approximately 2.74 Å for the x = 0.6 sample.

The comprehensive characterization reveals that optimal-trace LiCl addition (x = 0.6) enhances the atomic ordering while maintaining a small particle size in Pt_3Co nanoparticles. This dual functionality resolves the inherent conflict between thermal ordering and sintering in high-loading IMC synthesis.

3.2 Mechanism of LiCl-assisted synthesis

To investigate the role of LiCl in Pt_3Co atomic ordering evolution, a complementary $Pt_3Co/C(Li_x)$-T series (T = 200–700 °C; no hold time) was synthesized to understand the *ex situ* formation pathways of $Pt_3Co/C(Li_{0.0})$-700 °C-2 h and $Pt_3Co/C(Li_{0.6})$-700 °C-2 h. XRD analysis of $Pt_3Co/C(Li_{0.6})$ (Fig. 3a) reveals distinct diffraction peaks at 200 °C, indicating Pt/Co salt reduction and Pt nanoparticle formation. Subsequently, between 300 °C and 500 °C, all diffraction peaks shift toward higher angles (Table S5). This shift signifies Co salt reduction and diffusion into the Pt lattice. At 500–700 °C, the diffraction peaks align with the Pt_3Co (111), (200), (220), and (311) planes (PDF #29-0499), although the absence of low-angle peaks indicates Pt_3Co-IMC formation. After holding at 700 °C for 2 h, the

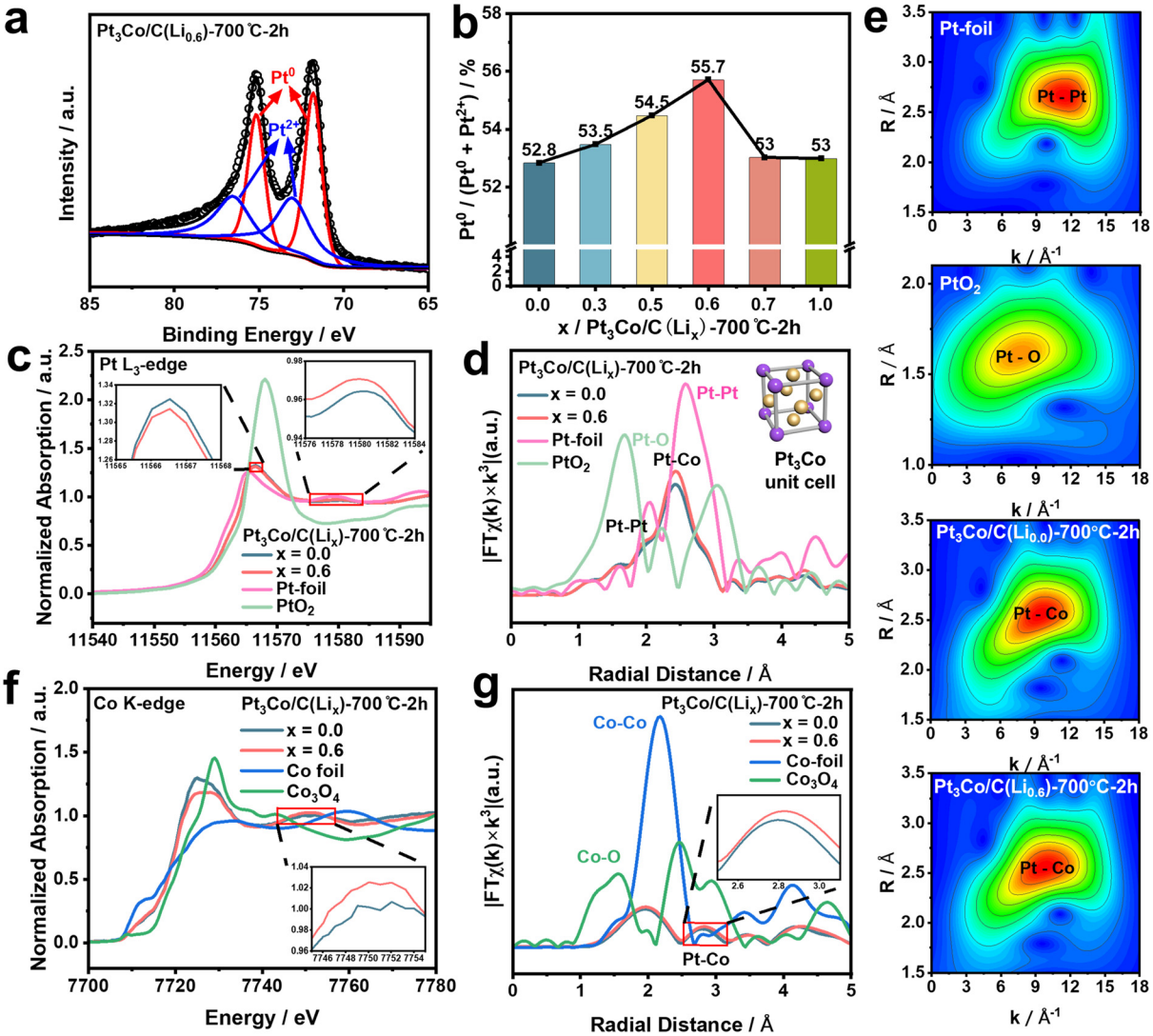

Fig. 2 Electronic structure characterization of $Pt_3Co/C(Li_x)$-700 °C-2 h catalysts. (a) High-resolution Pt 4f XPS spectrum with peak deconvolution for the x = 0.6 sample. (b) Histogram of Pt^0 content ($Pt^0/(Pt^0 + Pt^{2+})$) across the $Pt_3Co/C(Li_x)$-700 °C-2 h catalyst series. (c) Pt L_3-edge normalized XANES spectra for Pt foil, PtO_2, $Pt_3Co/C(Li_{0.0})$-700 °C-2 h, and $Pt_3Co/C(Li_{0.6})$-700 °C-2 h samples. (d) FT-EXAFS spectra corresponding to the samples shown in (c). (e) Pt L_3-edge WT-EXAFS contour plots corresponding to the samples shown in (c). (f) Co K-edge normalized XANES spectra for Co foil, $Pt_3Co/C(Li_{0.0})$-700 °C-2 h, and $Pt_3Co/C(Li_{0.6})$-700 °C-2 h samples. (g) FT-EXAFS spectra corresponding to the samples shown in (f).

emergence of strong diffraction peaks at Pt_3Co (100) and (110) planes suggests increased structural ordering.

XRD analysis of $Pt_3Co/C(Li_{0.0})$ (Fig. S9) reveals a similar alloying evolution pathway to that of LiCl-assisted $Pt_3Co/C(Li_{0.6})$, albeit with critical distinctions. First, while unreduced Pt/Co salt persists in $Pt_3Co/C(Li_{0.0})$-200 °C, complete Pt/Co salt reduction occurs in $Pt_3Co/C(Li_{0.6})$-200 °C (Fig. S10). This indicates that the strong polarization force of LiCl lowers Pt/Co salt reduction energy barriers, facilitating its conversion.[42,50] Second, prior to Pt_3Co alloy formation, equivalent-temperature diffraction peaks for $Pt_3Co/C(Li_{0.6})$ consistently appear at higher angles than those of $Pt_3Co/C(Li_{0.0})$ (Table S5). This enhanced lattice contraction suggests that molten LiCl forms a liquid phase that accelerates Co migration and incorporation into the Pt lattice. This effect is exemplified at 500 °C, where Pt_3Co alloy formation is complete in $Pt_3Co/C(Li_{0.6})$ but remains undetectable in $Pt_3Co/C(Li_{0.0})$ (Fig. S15). Finally, isothermal holding at 600/700 °C for 2 h induces distinct ordering behavior. Particularly, $Pt_3Co/C(Li_{0.6})$-600 °C-2 h develops a weak (110) superlattice reflection, absent in $Pt_3Co/C(Li_{0.0})$-600 °C-2 h. These Li-dependent behaviors possibly correlate with the established vacancy-mediated restructuring mechanisms in Pt_3Co alloys.[51–55] Surface-initiated defects lower atomic migration barriers, initiating self-accelerated [110]-oriented reconstruction that propagates long-range order.[51,53,54] Building on this mechanism, we propose that the

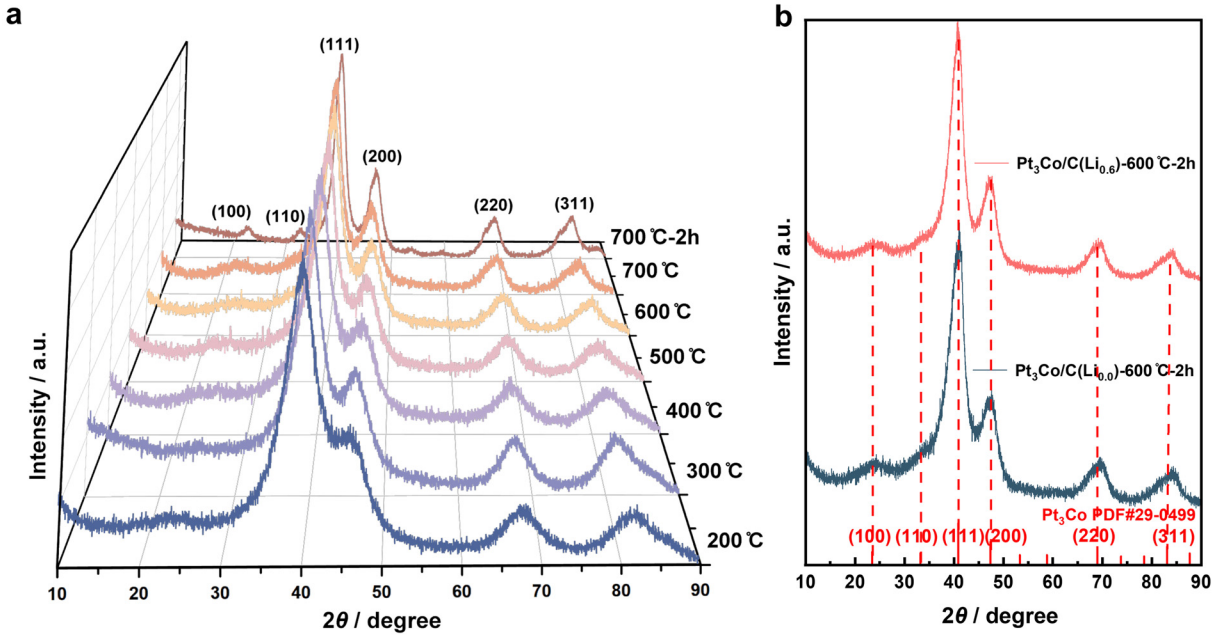

Fig. 3 XRD analysis of the structural evolution in Pt_3Co/C catalysts. (a) *Ex situ* XRD patterns tracking thermal progression during annealing of the $Pt_3Co/C(Li_{0.6})$ precursor toward $Pt_3Co/C(Li_{0.6})$-700 °C-2 h. (b) Comparative XRD analysis of $Pt_3Co/C(Li_{0.6})$ and $Pt_3Co/C(Li_{0.0})$ precursors following isothermal treatment (600 °C-2 h).

LiCl-derived liquid phase reduces the energy barriers for surface atom rearrangement, thereby enhancing Pt_3Co atomic ordering.

XAS provided further mechanistic insights into the ordering process. Pt L_3-edge X-ray absorption near-edge structure (XANES) spectra for $Pt_3Co/C(Li_{0.6})$ series (Fig. 4a) reveal a gradual attenuation of WL intensity with increasing temperature, indicating progressive reduction of Pt oxidation states toward Pt^0. The corresponding primary FT-EXAFS peak (Fig. 4b) reveals sequential structural evolution. At 300 °C, the main peak at 2.79 Å aligns with Pt–Pt bonds in Pt foil, confirming metallic Pt formation. As the temperature rises to 600 °C, the main peak shifts to ~2.74 Å, matching the Pt–Co bond distance and signaling alloy formation. During the 700 °C-2 h hold, the main peak intensity increases significantly without positional shift, indicating ordering development. Quantitative EXAFS fitting analysis (Fig. S11 and Table S4) confirms this progression. The $Pt_3Co/C(Li_{0.6})$-300 °C catalyst exhibits coexisting Pt–O, Pt-Cl, and Pt–Pt coordination. At 600 °C, decreased Pt–O coordination and emergence of Pt–Co bonding accompany increased Pt–Pt coordination (CN = 8.69). Finally, the $Pt_3Co/C(Li_{0.6})$-700 °C-2 h catalyst displays significantly enhanced Pt–Co coordination and Pt–Pt coordination, confirming the development of the ordered structure.

Complementary XAS analysis of $Pt_3Co/C(Li_{0.0})$ (Fig. S12, S13 and Table S4) reveals similar thermal evolution but with attenuated signals compared to the LiCl-assisted analogue. A direct comparison of Pt L_3-edge spectra (Fig. 4c–h) elucidates the role of LiCl. At 300 °C, $Pt_3Co/C(Li_{0.0})$-300 °C exhibits lower white-line intensity *versus* $Pt_3Co/C(Li_{0.6})$-300 °C (Fig. 4c). This contradiction is resolved by FT-EXAFS (Fig. 4d), which exhibits dominant peaks at 1–2 Å for $Pt_3Co/C(Li_{0.0})$-300 °C, characteristic of Pt–O bonds in PtO_2-like species. In contrast, $Pt_3Co/C(Li_{0.6})$-300 °C exhibits metallic Pt features. WT-EXAFS analysis further confirms this phase difference. $Pt_3Co/C(Li_{0.0})$-300 °C shows intensity maxima at 2.0 Å (Pt–O/Pt–Cl scattering), while $Pt_3Co/C(Li_{0.6})$-300 °C exhibits a maximum at 2.7 Å (Pt–Pt scattering) (Fig. 4e), demonstrating LiCl-assisted Pt/Co salt reduction. At 600 °C, $Pt_3Co/C(Li_{0.6})$-600 °C exhibits reduced WL intensity (Fig. 4f) *versus* $Pt_3Co/C(Li_{0.0})$-600 °C, indicating a lower Pt valence state due to enhanced Co diffusion into the Pt lattice and subsequent electron transfer from the less electronegative Co to the more electronegative Pt. FT-EXAFS (Fig. 4g) reveals that both samples share a ~2.75 Å Pt–Co peak, but $Pt_3Co/C(Li_{0.6})$-600 °C exhibits higher intensity, corresponding to a higher CN (Table S4). WT-EXAFS (Fig. 4h) further shows reduced oxide signatures in $Pt_3Co/C(Li_{0.6})$-600 °C, verifying ordered alloy formation.

Based on the comprehensive XRD and XAS analyses, trace LiCl facilitates Pt_3Co nanoparticle ordering with constrained size through a synergistic three-stage mechanism that reduces critical energy barriers (Fig. 5). Stage 1: enhancing Pt/Co salt reduction. The polarization force of LiCl lowers the reduction energy barriers for the Pt/Co salt, enabling complete conversion to metallic Pt in $Pt_3Co/C(Li_{0.6})$ at 200 °C. In contrast, $Pt_3Co/C(Li_{0.0})$ retains unreduced oxides at 200 °C. This foundational step supplies the requisite metallic species for subsequent alloying while avoiding excessive temperatures that drive particle growth. Stage 2: accelerating alloy formation. The LiCl-derived liquid phase drastically reduces the Co

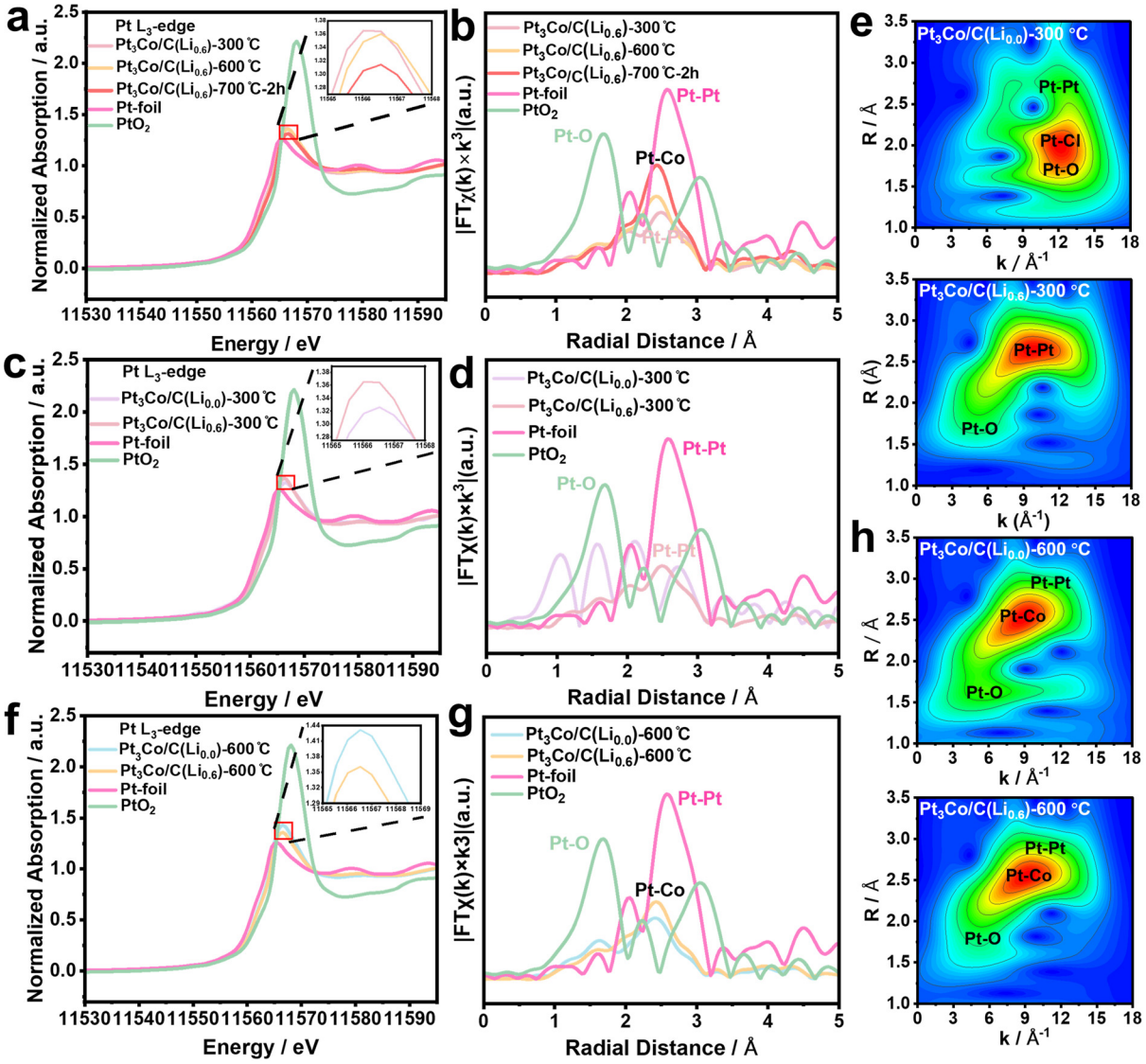

Fig. 4 XAS analysis of the structural evolution in Pt_3Co/C catalysts. (a) Pt L_3-edge normalized XANES spectra of Pt foil, PtO_2, and $Pt_3Co/C(Li_{0.6})$ precursor annealed at 300 °C, 600 °C, and 700 °C for 2 h. (b) Corresponding FT-EXAFS spectra of (a). (c) Comparative normalized Pt L_3-edge XANES spectra of Pt foil, PtO_2, $Pt_3Co/C(Li_{0.0})$-300 °C, and $Pt_3Co/C(Li_{0.6})$-300 °C. (d) Corresponding FT-EXAFS spectra of (c). (e) Pt L_3-edge WT-EXAFS contour plots of $Pt_3Co/C(Li_{0.0})$-300 °C and $Pt_3Co/C(Li_{0.6})$-300 °C. (f) Comparative Pt L_3-edge normalized XANES spectra of Pt foil, PtO_2, $Pt_3Co/C(Li_{0.0})$-600 °C, and $Pt_3Co/C(Li_{0.6})$-600 °C. (g) Corresponding FT-EXAFS spectra of (f). (h) WT-EXAFS contour plots of $Pt_3Co/C(Li_{0.0})$-600 °C and $Pt_3Co/C(Li_{0.6})$-600 °C.

diffusion barriers. This promotes rapid Co incorporation into the Pt lattice, as evidenced by enhanced lattice contraction and the emergence of Pt–Co bonding. This accelerated alloying, occurring at a lower temperature (500 °C) than possible without LiCl (600 °C), is an essential precursor step for atomic ordering and crucially minimizes the time spent at high temperatures, thereby limiting undesirable particle agglomeration or Ostwald ripening. Stage 3: promoting surface atomic rearrangement. LiCl reduces the energy barrier for the atomic rearrangement necessary for ordering. During isothermal holding (700 °C), it promotes surface restructuring, generating vacancies and defects that lower diffusion barriers and initiate a self-accelerating, [110]-oriented reconstruction process. This leads to the development of long-range order, manifested by the emergence of superlattice reflections ((100), (110)) in $Pt_3Co/C(Li_{0.6})$ and significantly enhanced Pt–Co/Pt–Pt CNs after the 700 °C hold, which are effects absent or attenuated in the control sample. Collectively, this barrier-lowering cascade (reduction → alloying → ordering) enables efficient synthesis of structurally ordered Pt_3Co nanoparticles with minimized coarsening.

Building upon the proposed LiCl-mediated mechanism, this strategy is expected to be extendable to other PtM-IMCs, such as PtFe, PtNi, PtZn, and even more complex multi-metal-

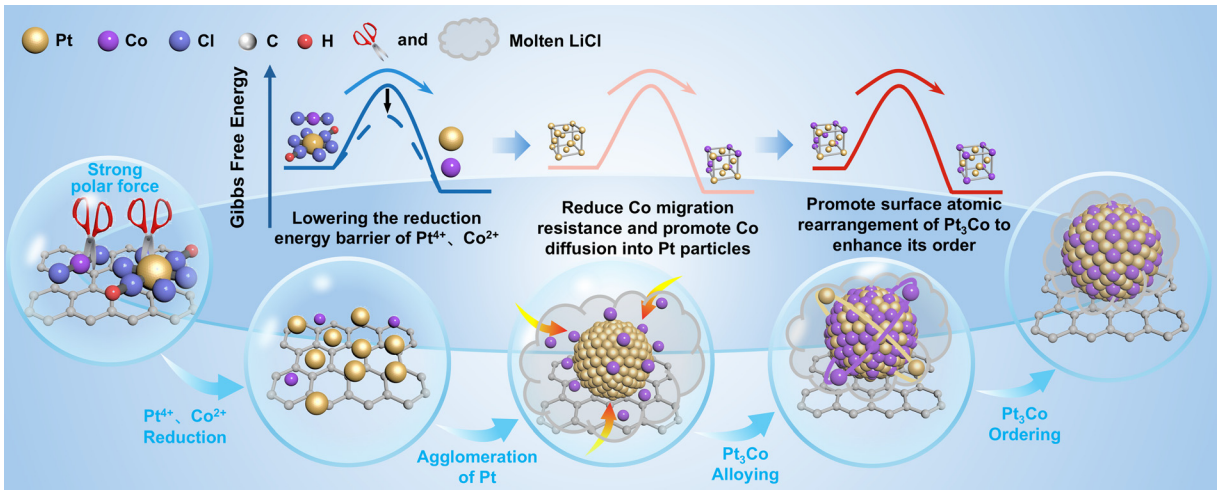

Fig. 5 Proposed mechanism for LiCl-assisted structural evolution during Pt_3Co nanoparticle synthesis. Schematic illustrating the triple role of trace LiCl in reducing energy barriers across three critical stages: (I) enhanced Pt/Co salt reduction at lower temperatures. (II) 500–600 °C, accelerated alloy formation *via* liquid-phase diffusion. (III) 600–700 °C, promoted surface rearrangement, collectively enabling the efficient formation of structurally ordered Pt_3Co nanoparticles with minimized coarsening.

lic compounds, as these systems generally exhibit alloying and ordering behaviors analogous to those observed in the Pt_3Co system.[56–61] Nevertheless, owing to intrinsic differences in reduction potentials, diffusion kinetics, and alloying thermodynamics among various transition metals, the optimal temperatures and thermal treatment conditions may vary. Further investigations are currently underway within our group to explore and optimize these extensions.

3.3 ORR electrocatalysis and MEA application

After washing the $Pt_3Co/C(Li_{0.6})$-700 °C-2 h catalyst with DI water, the Li element content decreased from 0.21 wt% to 0.013 wt% (Table S1). Therefore, it is concluded that LiCl has been removed by water washing and will not affect subsequent electrochemical testing.

CV curves of the $Pt_3Co/C(Li_x)$-700 °C-2 h series (x = 0.0–1.0) (Fig. 6a) reveal decreasing H_2 underpotential deposition (H_{UPD}) regions (0.05–0.45 V *vs.* RHE) with increasing Li content, corresponding to declining ECSAs from 52.62 ± 0.39, 52.13 ± 0.24, 50.32 ± 0.81, 49.23 ± 0.61, 48.97 ± 0.28, to 48.41 ± 0.49 $m^2\ g_{Pt}^{-1}$ (Table S6). This result indicates progressive particle growth, aligning with the TEM-determined size increases. The SCV curves (Fig. 6b) confirm the superiority of the various catalysts. Half-wave potential ($E_{1/2}$ *vs.* RHE), MAs (at 0.9 V *vs.* RHE), and SAs (at 0.9 V *vs.* RHE) exhibit a volcano-type relationship with LiCl content (x) (Fig. 6c and Table S6), reaching maximum values of 0.934 ± 0.004 V, 0.86 ± 0.04 A mg_{pt}^{-1}, and 1.75 ± 0.07 mA cm^{-2}, respectively, at x = 0.6. This activity enhancement correlates directly with structural advantages, such as higher ordering and a Pt^0-rich surface.

ADT reveals the superior stability of $Pt_3Co/C(Li_{0.6})$-700 °C-2 h compared to the $Pt_3Co/C(Li_{0.0})$-700 °C-2 h control (Fig. 6d–f). Following ADT, the x = 0.6 sample exhibits only a 3.28% loss in ECSA and a minimal negative shift in $E_{1/2}$ of 7.7 mV, significantly lower than the corresponding losses of 9.8% and 10.32 mV for the x = 0.0 control. Similarly, MA and SA retention is markedly better for the x = 0.6 sample (29.3% MA decrease, 26.7% SA decrease) *versus* the x = 0.0 control (34.4% MA decrease, 28.4% SA decrease). This enhanced durability is primarily attributed to the improved atomic ordering in the x = 0.6 catalyst. Complementary TEM analysis (Fig. S14) reveals pronounced particle coalescence in the x = 0.0 control, with the mean size increasing from 3.11 ± 0.03 to 3.79 ± 0.11 nm, indicating extensive Ostwald ripening of Pt nanoparticles during cycling. In contrast, the x = 0.6 catalyst demonstrates exceptional structural integrity with negligible growth (3.58 ± 0.02 to 3.59 ± 0.06 nm). This suppressed coalescence is consistent with its ECSA retention and further confirms the enhanced resistance against Pt oxidation and dissolution.

To evaluate the application potential in PEMFCs, MEAs with low Pt loading (0.1 $mg_{Pt}\ cm^{-2}$) were fabricated using $Pt_3Co/C(Li_{0.6})$-700 °C-2 h and benchmarked against $Pt_3Co/C(Li_{0.0})$-700 °C-2 h. Steady-state H_2–air polarization curves (Fig. 6g) demonstrate the superior performance of the x = 0.6 catalyst, achieving a PPD of 1.23 W cm^{-2} *versus* 1.19 W cm^{-2} for x = 0.0 control. Crucially, at 0.80 V, the x = 0.6 catalyst reaches a current density of 0.54 A cm^{-2}, 59% higher than the x = 0.0 control (0.34 A cm^{-2}), and exceeding the DOE target (0.30 A cm^{-2}). Under a practical operating potential of 0.65 V, the x = 0.6 sample yields a current density of 1.67 A cm^{-2}, outperforming the x = 0.0 control (1.48 A cm^{-2}). Under H_2–O_2 conditions (Fig. 6h), the x = 0.6 sample reaches a PPD of 2.92 W cm^{-2}, surpassing that of the x = 0.0 control (2.64 W cm^{-2}) by 10.6%, again evidencing the boosted ORR activity. At 0.9 V *vs.* RHE, the x = 0.6 sample exhibits an MA of 0.61 A mg_{pt}^{-1}, 27% higher than that of the x = 0.0 control (0.48 A mg_{pt}^{-1}). Under H_2–N_2 conditions (Fig. S15), the ECSA of the x = 0.6 catalyst

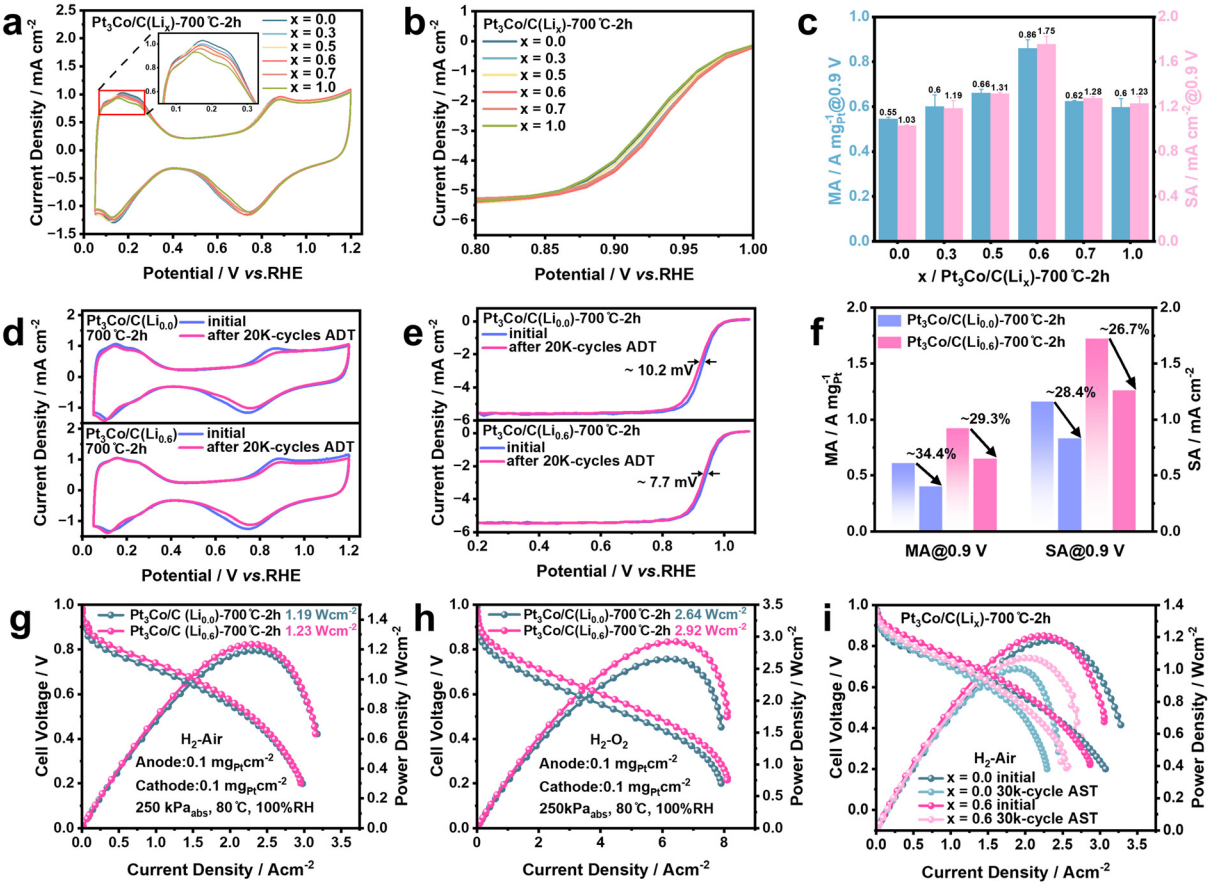

Fig. 6 Electrochemical characterization and fuel cell performance of $Pt_3Co/C(Li_x)$-700 °C-2 h catalysts. (a) Comparison of CV curves for $Pt_3Co/C(Li_x)$-700 °C-2 h catalysts. (b) ORR polarization curves (*iR*-compensated). (c) MA and SA at 0.9 V *vs.* RHE. (d and e) Comparative CVs and ORR polarization curves for $Pt_3Co/C(Li_{0.6})$-700 °C-2 h and $Pt_3Co/C(Li_{0.0})$-700 °C-2 h catalysts before and after ADT. (f) Corresponding MA/SA retention after ADT. (g and h) Steady-state polarization curves under H_2–air and H_2–O_2 conditions for $Pt_3Co/C(Li_{0.6})$-700 °C-2 h and $Pt_3Co/C(Li_{0.0})$-700 °C-2 h catalysts. (i) H_2-air polarization curves before and after 30k-cycle AST under U.S. DOE protocols.

(71.31 m^2 g-1 Pt) is 13.56% lower than that of the control (82.50 m^2 g_{Pt}^{-1}), attributed to a slight increase in particle size. EIS was employed to analyze the charge transfer resistance ($R_{ct\text{-}c}$) of the MEAs at 0.1 and 1.2 A cm^{-2} (Fig. S16), which provides insights into the catalytic activity of the cathode catalyst.[23] At both 0.1 and 1.2 A cm^{-2}, the $Pt_3Co/C(Li_{0.6})$-700 °C-2 h catalyst exhibits lower $R_{ct\text{-}c}$ values than the $Pt_3Co/C(Li_{0.0})$-700 °C-2 h catalyst (2.23 *vs.* 2.27 Ω cm^2; 0.25 *vs.* 0.39 Ω cm^2, Table S7), indicating more efficient charge transfer and intrinsically enhanced ORR kinetics. However, at 1.2 A cm^{-2}, the $Pt_3Co/C(Li_{0.6})$-700 °C-2 h catalyst exhibits a higher mass transport resistance (R_{mt}) (0.42 *vs.* 0.23 Ω cm^2), implying hindered reactant diffusion under high-current operation. Consequently, targeted optimization of the triple-phase boundary structure remains crucial for further improving cell performance.

Notably, at a cathode Pt loading of 0.33 mg_{Pt} cm^{-2}, the x = 0.6 sample achieves a MA of 0.57 A mg_{pt}^{-1} at 0.9 V, significantly surpassing the 0.21 A mg_{pt}^{-1} of the x = 0.0 control. This performance advantage extends to the PPD, with the x = 0.6 catalyst reaching 1.21 W cm^{-2} in H_2–air and 3.08 W cm^{-2} in H_2–O_2, compared to the 1.18 and 2.92 W cm^{-2} for the control, respectively. However, these PPD values show no significant increase compared to those under the corresponding low Pt loading conditions. To elucidate this phenomenon, the polarization behavior of the sample at x = 0.6 under different loadings was analyzed in H_2–air. The MA at 0.9 V remains nearly identical (0.61 *vs.* 0.57 A mg_{pt}^{-1}), suggesting that electrochemical kinetics are not the limiting factor. As shown in Fig. S17, the ohmic losses (η_{ohmic}) and mass-transport losses ($\eta_{mass\ transport}$) are derived from the differences between the measured voltage (E_{cell}) and the internal-resistance-corrected voltage ($E_{iR\text{-}free}$), and between the $E_{iR\text{-}free}$ and $\log j_k - E$ curve (j_k is the extrapolated kinetic current obtained using Tafel analysis). At 1000 mA cm^{-2} ($\log j$ = 3), the η_{ohmic} values are 38.4 and 28.6 mV, while the corresponding $\eta_{mass\ transport}$ values are 57.3 and 88.9 mV for $MEA_{0.10\ mg_{Pt}\ cm^{-2}}$ (Pt loading is 0.10 mg_{Pt} cm^{-2}) and $MEA_{0.33\ mg_{Pt}\ cm^{-2}}$ (Pt loading is 0.33 mg_{Pt} cm^{-2}), respectively. The $\eta_{mass\ transport}$ in high Pt-loading electrodes is approximately 30 mV higher than that in low-loading electrodes, indicating that the performance loss is primarily attributed to mass transport rather than ohmic resistance. This is pri-

marily attributed to the thicker catalyst layer in high-loading configurations, which impedes O_2 diffusion through the ionomer film and porous network,[30,33] while increased water generation aggravates flooding and restricts reactant accessibility. Consequently, the performance benefit from higher Pt loading is offset by enhanced mass-transport losses, which ultimately cap the achievable PPD despite the catalyst's high intrinsic activity. Nevertheless, high-loading MEAs are preferred for durability tests, as they ensure sufficient catalyst utilization during extended operation and allow a more reliable assessment of the intrinsic structural and compositional stability of the catalyst, while minimizing artifacts arising from transport limitations caused by carbon network degradation.

AST following the U. S. DOE protocol (0.33 mg_{Pt} cm^{-2}) reveals the superior durability of the x = 0.6 catalyst. After 30k-cycles (Fig. 6i), the x = 0.6 catalyst exhibits lower voltage drops than the x = 0.0 control across all operational current densities. Its PPD in H_2–air retains 88.4% of its initial PPD (1.07 W cm^{-2} *vs.* initial 1.21 W cm^{-2}), exceeding the x = 0.0 catalyst retention (1.00 W cm^{-2} *vs.* initial 1.18 W cm^{-2}). This enhanced stability is corroborated under H_2–O_2 conditions (Fig. S18), where the x = 0.6 catalyst maintains 87.9% PPD retention (2.71 *vs.* initial 3.08 W cm^{-2}) *versus* 87.3% for the control (2.52 *vs.* 2.92 W cm^{-2}). The MA of the x = 0.6 catalyst at 0.9 V retains 80.7% (0.57 *vs.* 0.46 A mg_{pt}^{-1}), and the MA of the x = 0.0 catalyst retains 85.7% (0.21 *vs.* 0.18 A mg_{pt}^{-1}).

Complementary kinetic analysis (Fig. S19) reveals that the x = 0.6 catalyst exhibits the lowest initial Tafel slope (51.67 mV dec^{-1}), confirming enhanced ORR kinetics from the ordered Pt_3Co structure. After AST, its Tafel slope increases minimally (+4.08% to 53.78 mV dec^{-1}), outperforming the degradation of control (+5.83% to 61.01 mV dec^{-1} from 57.65 mV dec^{-1}). Mechanistic insights from ECSA measurements (Fig. S20) show superior structural stability. The x = 0.6 catalyst experiences a 41.8% ECSA loss (72.53 to 42.21 m^2 g_{Pt}^{-1}) *versus* the 46.5% for the control (88.54 to 47.34 m^2 g_{Pt}^{-1}). Direct morphological evidence from TEM (Fig. S21) confirms significantly mitigated particle coarsening in the x = 0.6 catalyst (mean size: 3.58 ± 0.02 to 5.58 ± 0.19 nm, +56% growth) relative to severe Ostwald ripening in the control (3.11 ± 0.03 to 5.97 ± 0.22 nm, +92% growth).

Collectively, these findings establish that LiCl-assisted Pt_3Co/C demonstrates exceptional performance in PEMFC operational environments, with performance metrics ranking among the highest reported for Pt-based catalysts (Table S8), positioning this material as a leading candidate for next-generation fuel cell applications.

4. Conclusions

In summary, we established a trace LiCl-assisted synthesis strategy enabling a high-loading (50.43 wt% Pt), small-particle (3.58 nm) $Pt_3Co/C(Li_{0.6})$-700 °C-2 h catalyst with exceptional atomic ordering. Through comprehensive characterization, we elucidated LiCl's triple-function mechanism: enhancing Pt/Co salt reduction, accelerating alloy formation *via* liquid-phase diffusion, and promoting surface rearrangement, collectively enabling efficient formation of structurally ordered Pt_3Co nanoparticles with minimized coarsening. The resulting Pt_3Co/C catalyst achieves an MA of 0.61 A mg_{pt}^{-1} at 0.9 V, 39% above DOE 2025 targets, at 80 °C in PEMFCs, with a PPD of 2.92 W cm^{-2} (H_2–O_2) and 1.23 W cm^{-2} (H_2–air), and remarkable stability (88.4% PPD retention after 30k-cycle AST). This work resolved the fundamental ordering-sintering trade-off in IMC synthesis, providing mechanistic insights into liquid-phase-mediated diffusion control for manufacturing high-performance catalysts that meet next-generation energy conversion demands.

Author contributions

Yutao Ni: writing – original draft, methodology, investigation, data curation and visualization. Jiahui Song: investigation and data curation. Huiying Lan: resources and investigation. Xue Jing: resources and investigation. Wenwen Shi: methodology, visualization, supervision and funding acquisition. Ruimin Ding: supervision, investigation, writing – review & editing, visualization, and conceptualization. Xi Yin: conceptualization, methodology, writing – review & editing, supervision, and funding acquisition.

Conflicts of interest

The authors declare that they have no known competing financial interests or personal relationships that could have appeared to influence the work reported in this paper.

Data availability

The data that support the findings of this study are available in the supplementary information (SI). Supplementary information: detailed description including the supporting figures and tables. See DOI: https://doi.org/10.1039/d5gc05077d.

Acknowledgements

This research was supported by the National Key Research and Development Program of China (Grant No. 2021YFB4001203), the National Natural Science Foundation of China (Grant No. 22572211 and 22509216), the Youth Talent Development Program of SKLCC (Grant No. 2025BWZ012), and the Fundamental Research Program of Shanxi Province (No. 202203021212007). We thank the facility for the support of the BL14W1-XAFS beamline of the SSRF.

References

1 Z. Lin, N. Sathishkumar, Y. Xia, S. Li, X. Liu, J. Mao, H. Shi, G. Lu, T. Wang, H.-L. Wang, Y. Huang, L. Elbaz and Q. Li, *Angew. Chem., Int. Ed.*, 2024, **63**, e202400751.

2 W. Xu, Z. Zhu, Y. Wang, P. Cui, L. Tong, K. Zhao, J. Yuan, Z.-Y. Zhou, H.-W. Liang, N. Tian and S.-G. Sun, *J. Mater. Chem. A*, 2023, **11**, 4078–4087.

3 H. Guo, P. Zhang, S. Huang, M. Li, G. Sun, J. Li, Y. Lin, B. Liu and Y. Pan, *Nano Res. Energy*, 2025, **4**, e9120144.

4 J. Liang, Z. Zhao, N. Li, X. Wang, S. Li, X. Liu, T. Wang, G. Lu, D. Wang, B. Hwang, Y. Huang, D. Su and Q. Li, *Adv. Energy Mater.*, 2020, **10**, 2000179.

5 X. Liu, J. Liang and Q. Li, *Chin. J. Catal.*, 2023, **45**, 17–26.

6 Y. Nie, L. Li and Z. Wei, *Chem. Soc. Rev.*, 2015, **44**, 2168–2201.

7 Z. Qi, C. Xiao, C. Liu, T. W. Goh, L. Zhou, R. Maligal-Ganesh, Y. Pei, X. Li, L. A. Curtiss and W. Huang, *J. Am. Chem. Soc.*, 2017, **139**, 4762–4768.

8 J. Li, S. Sharma, K. Wei, Z. Chen, D. Morris, H. Lin, C. Zeng, M. Chi, Z. Yin, M. Muzzio, M. Shen, P. Zhang, A. A. Peterson and S. Sun, *J. Am. Chem. Soc.*, 2020, **142**, 19209–19216.

9 J. Liang, F. Ma, S. Hwang, X. Wang, J. Sokolowski, Q. Li, G. Wu and D. Su, *Joule*, 2019, **3**, 956–991.

10 J. Li, Z. Xi, Y.-T. Pan, J. S. Spendelow, P. N. Duchesne, D. Su, Q. Li, C. Yu, Z. Yin, B. Shen, Y. S. Kim, P. Zhang and S. Sun, *J. Am. Chem. Soc.*, 2018, **140**, 2926–2932.

11 P. Strasser, S. Koh, T. Anniyev, J. Greeley, K. More, C. Yu, Z. Liu, S. Kaya, D. Nordlund, H. Ogasawara, M. F. Toney and A. Nilsson, *Nat. Chem.*, 2010, **2**, 454–460.

12 J. Liang, Y. Wan, H. Lv, X. Liu, F. Lv, S. Li, J. Xu, Z. Deng, J. Liu, S. Zhang, Y. Sun, M. Luo, G. Lu, J. Han, G. Wang, Y. Huang, S. Guo and Q. Li, *Nat. Mater.*, 2024, **23**, 1259–1267.

13 Y. Hu, M. Zhu, X. Luo, G. Wu, T. Chao, Y. Qu, F. Zhou, R. Sun, X. Han, H. Li, B. Jiang, Y. Wu and X. Hong, *Angew. Chem.*, 2021, **133**, 6607–6612.

14 Y. Wang, X. Lei, J. Zhao, X. Liu, L. Zhang and D. Su, *J. Mater. Res.*, 2024, **39**, 1325–1343.

15 J. Zhang, L. Zhang and Z. Cui, *Chem. Commun.*, 2021, **57**, 11–26.

16 X.-F. Han, N. Batool, W.-T. Wang, H.-T. Teng, L. Zhang, R. Yang and J.-H. Tian, *ACS Appl. Mater. Interfaces*, 2021, **13**, 37133–37141.

17 Q. Li, L. Wu, G. Wu, D. Su, H. Lv, S. Zhang, W. Zhu, A. Casimir, H. Zhu, A. Mendoza-Garcia and S. Sun, *Nano Lett.*, 2015, **15**, 2468–2473.

18 J. Liang, Z. Zhao, N. Li, X. Wang, S. Li, X. Liu, T. Wang, G. Lu, D. Wang, B.-J. Hwang, Y. Huang, D. Su and Q. Li, *Adv. Energy Mater.*, 2020, **10**, 2000179.

19 S. Yang, J. Kim, Y. J. Tak, A. Soon and H. Lee, *Angew. Chem.*, 2016, **55**, 2058–2062.

20 S. Shin, E. Lee, J. Nam, J. Kwon, Y. Choi, B. J. Kim, H. C. Ham and H. Lee, *Adv. Energy Mater.*, 2024, **14**, 2400599.

21 X. Cao, H. Guo, Y. Han and M. Li, *Nat. Commun.*, 2025, **16**, 2851.

22 X. Geng, M. Vega-Paredes, X. Lu, P. Chakraborty, Y. Li, C. Scheu, Z. Wang and B. Gault, *Adv. Mater.*, 2024, **36**, 2404839.

23 M. I. Maulana, T. H. Jo, H.-Y. Lee, C. Lee, C. Gyan-Barimah, C.-H. Shin, J.-H. Yu, K.-S. Lee, S. Back and J.-S. Yu, *J. Am. Chem. Soc.*, 2024, **146**, 30922–30932.

24 C.-L. Yang, L.-N. Wang, P. Yin, J. Liu, M.-X. Chen, Q.-Q. Yan, Z.-S. Wang, S.-L. Xu, S.-Q. Chu, C. Cui, H. Ju, J. Zhu, Y. Lin, J. Shui and H.-W. Liang, *Science*, 2021, **374**, 459–464.

25 M. Wang, E. Sun, S. Zhao, Y. Sun, S. Zhang, Z. Li and M. Wu, *J. Colloid Interface Sci.*, 2025, **682**, 115–123.

26 J. Liang, L. Liang, B. Zeng, B. Feng, L. Du, X. Qiu, Y. Wang, H. Song, S. Liao, M. Shao and Z. Cui, *Angew. Chem., Int. Ed.*, 2024, **63**, e202412825.

27 H.-G. Jo, K.-H. Kim and H.-J. Ahn, *Appl. Surf. Sci.*, 2021, **554**, 149594.

28 L. Tian, X. Gao, M. Zhu, Z. Huang, B. Wu, C. Chen, X. Ma, Y. Ruan, W. Guo, X. Meng, H. Wang, W. Du, S. He, H. Pan, X. Zheng, Z. Wu, H. Zhou, J. Xia and Y. Wu, *Adv. Mater.*, 2025, **37**, 2417095.

29 W. Zhang, X. Feng, Z. X. Mao, J. Li and Z. Wei, *Adv. Funct. Mater.*, 2022, **32**, 2204110.

30 Y. Xiong, L. Xiao, Y. Yang, F. J. DiSalvo and H. D. Abruña, *Chem. Mater.*, 2018, **30**, 1532–1539.

31 R. Zhang, T. Min, Y. Liu, L. Chen and W.-Q. Tao, *Int. J. Hydrogen Energy*, 2021, **46**, 20037–20053.

32 P. Yin, L.-J. Zuo, W.-J. Zeng, M. Zuo, L. Tong, X.-Z. Fu and H.-W. Liang, *Appl. Catal., B*, 2023, **328**, 122543.

33 Q. Cheng, S. Yang, C. Fu, L. Zou, Z. Zou, Z. Jiang, J. Zhang and H. Yang, *Energy Environ. Sci.*, 2022, **15**, 278–286.

34 L. Chen, W. Zhao, Y. Ren, Z. Liu, L. Zhang, Z. An, Y. Jia, C. Li, M. Xu, N. Zhang, Y. Zhang, K. Xie and M. Chai, *J. Electrochem. Soc.*, 2024, **171**, 094509.

35 G. A. Tritsaris, J. Greeley, J. Rossmeisl and J. K. Nørskov, *Catal. Lett.*, 2011, **141**, 909–913.

36 F. J. Perez-Alonso, D. N. McCarthy, A. Nierhoff, P. Hernandez-Fernandez, C. Strebel, I. E. L. Stephens, J. H. Nielsen and I. Chorkendorff, *Angew. Chem., Int. Ed.*, 2012, **51**, 4641–4643.

37 D. Takimoto, S. Toma, Y. Suda, T. Shirokura, Y. Tokura, K. Fukuda, M. Matsumoto, H. Imai and W. Sugimoto, *Nat. Commun.*, 2023, **14**, 19.

38 Y. Wang, L. Li, M. Shen, R. Tang, J. Zhou, L. Han, X. Zhang, L. Zhang, G. Kim and J. Wang, *Adv. Sci.*, 2023, **10**, 2303693.

39 Y. Jiang, T. Fu, J. Liu, J. Zhao, B. Li and Z. Chen, *RSC Adv.*, 2022, **12**, 4805–4812.

40 W.-J. Zeng, C. Wang, Q.-Q. Yan, P. Yin, L. Tong and H.-W. Liang, *Nat. Commun.*, 2022, **13**, 7654.

41 S. Zaman, Y.-Q. Su, C.-L. Dong, R. Qi, L. Huang, Y. Qin, Y.-C. Huang, F.-M. Li, B. You, W. Guo, Q. Li, S. Ding and B. Yu Xia, *Angew. Chem., Int. Ed.*, 2022, **61**, e202115835.

42 M. Xiao, L. Zhang, B. Luo, M. Lyu, Z. Wang, H. Huang, S. Wang, A. Du and L. Wang, *Angew. Chem., Int. Ed.*, 2020, **59**, 7230–7234.

43 C. Yan, Y. Zhu, Z. Fang, C. Lv, X. Zhou, G. Chen and G. Yu, *Adv. Energy Mater.*, 2018, **8**, 1800762.
44 D. Wang, H. L. Xin, R. Hovden, H. Wang, Y. Yu, D. A. Muller, F. J. DiSalvo and H. D. Abruña, *Nat. Mater.*, 2013, **12**, 81–87.
45 Y. Chen, Z. Meng, F. Liu, A. Zhang, X. Wang, Y. Xiong, H. Tang, T. Tian and H. Tang, *Adv. Funct. Mater.*, 2024, **34**, 2408383.
46 M. Luo, Z. Zhao, Y. Zhang, Y. Sun, Y. Xing, F. Lv, Y. Yang, X. Zhang, S. Hwang, Y. Qin, J.-Y. Ma, F. Lin, D. Su, G. Lu and S. Guo, *Nature*, 2019, **574**, 81–85.
47 J. Liang, Z. Zhao, N. Li, X. Wang, S. Li, X. Liu, T. Wang, G. Lu, D. Wang, B. Hwang, Y. Huang, D. Su and Q. Li, *Adv. Energy Mater.*, 2020, **10**, 2000179.
48 M. Luo and S. Guo, *Nat. Rev. Mater.*, 2017, **2**, 17059.
49 Y. Pan, Y. Chen, Y. Li, M. Liu, L. Yao, H. Zhao, X. Zhao, Z. Yue, S. Gui, Y. Chen, Q. Cheng and H. Yang, *Adv. Funct. Mater.*, 2025, 2503628.
50 D. Chen and S. Mu, *Adv. Mater.*, 2024, **36**, 2408285.
51 Y. Yan, J. S. Du, K. D. Gilroy, D. Yang, Y. Xia and H. Zhang, *Adv. Mater.*, 2017, **29**, 1605997.
52 H. Y. Kim, S. Cho, Y. J. Sa, S.-M. Hwang, G.-G. Park, T. J. Shin, H. Y. Jeong, S.-D. Yim and S. H. Joo, *Small*, 2016, **12**, 5347–5353.
53 Q. Li, L. Wu, G. Wu, D. Su, H. Lv, S. Zhang, W. Zhu, A. Casimir, H. Zhu, A. Mendoza-Garcia and S. Sun, *Nano Lett.*, 2015, **15**, 2468–2473.
54 H. Rong, J. Mao, P. Xin, D. He, Y. Chen, D. Wang, Z. Niu, Y. Wu and Y. Li, *Adv. Mater.*, 2016, **28**, 2540–2546.
55 F. Li, Y. Zong, Y. Ma, M. Wang, W. Shang, P. Tao, C. Song, T. Deng, H. Zhu and J. Wu, *ACS Nano*, 2021, **15**, 5284–5293.
56 Y. Ma, J. Peng, J. Tian, W. Gao, J. Xu, F. Li, P. Tieu, H. Hu, Y. Wu, W. Chen, L. Pan, W. Shang, P. Tao, C. Song, H. Zhu, X. Pan, T. Deng and J. Wu, *Sci. Adv.*, 2024, **10**, eado4935.
57 J. Li, Z. Xi, Y.-T. Pan, J. S. Spendelow, P. N. Duchesne, D. Su, Q. Li, C. Yu, Z. Yin, B. Shen, Y. S. Kim, P. Zhang and S. Sun, *J. Am. Chem. Soc.*, 2018, **140**, 2926–2932.
58 X. Han, Y. Zhou, X. Tai, G. Wu, C. Chen, X. Hong, L. Tong, F. Xu, H.-W. Liang and Y. Lin, *Nat. Commun.*, 2024, **15**, 7200.
59 G. Wang, J. Zhao, X. Chen, L. Niu, W. Zhang and X. Wang, *Int. J. Hydrogen Energy*, 2024, **64**, 309–317.
60 Z. Qi, C. Xiao, C. Liu, T. W. Goh, L. Zhou, R. Maligal-Ganesh, Y. Pei, X. Li, L. A. Curtiss and W. Huang, *J. Am. Chem. Soc.*, 2017, **139**, 4762–4768.
61 Q. Zhang, T. Shen, M. Song, S. Wang, J. Zhang, X. Huang, S. Lu and D. Wang, *J. Energy Chem.*, 2023, **86**, 158–166.